

# Simulations of 3D DC Borehole Resistivity Measurements with a Goal-Oriented *hp* Finite-Element Method. Part II: Through-Casing Resistivity Instruments

D. Pardo<sup>1</sup>, C. Torres-Verdín<sup>1</sup>, and M. Paszynski<sup>2</sup>

<sup>1</sup> Department of Petroleum and Geosystems Engineering, The University of Texas at Austin, TX, USA

<sup>2</sup> Department of Computer Science, Stanislaw Staszic University of Science and Technology in Krakow, Poland

The date of receipt and acceptance will be inserted by the editor

**Abstract** We simulate measurements acquired in steel-cased deviated wells at zero frequency (DC) for the assessment of rock formation properties. The assumed data acquisition configuration considers one transmitter and three receiver electrodes that are utilized to measure the second (vertical) difference of the electric potential. We assume a homogeneous 1.27 cm thick steel-casing with resistivity equal to  $10^{-5}\Omega\cdot\text{m}$ .

Simulations are performed with two different numerical methodologies. The first one is based on transferring two-dimensional (2D) axi-symmetric optimal grids to a three-dimensional (3D) simulation software. The second one produces automatically optimal 3D grids yielded by a 3D self-adaptive goal-oriented algorithm. Both method-

ologies utilize high-order finite elements (FE) that are specially well-suited for problems with high-contrast coefficients and rapid spatial variations of the electric field, as it occurs in simulations that involve steel-cased wells.

The methodology based on transferring 2D-optimal grids is efficient in terms of CPU time (few seconds per logging position). Unfortunately, it may produce inaccurate 3D-simulations, even though the error remains below 1% for the axi-symmetric (vertical) well. The methodology based on optimal 3D-grids, although less efficient in terms of CPU time (few hours per logging position), it produces accurate results that are verified by a built-in *a posteriori* error estimator.

Simulated measurements indicate that for a thirty-degrees deviated well, measurements in conductive layers ( $0.01\Omega\cdot\text{m}$ ) are similar to those obtained in vertical wells. However, in resistive layers ( $10000\Omega\cdot\text{m}$ ) we

---

*Correspondence to:* David Pardo, CPE 5.168A, Speedway and 26th, Austin, TX 78712, USA. e-mail: dzubiaur@gmail.com. Phone: (512) 471-3775.

observe 100% larger readings in the thirty-degrees deviated well. This difference becomes 3000% for the case of a sixty-degrees deviated well. For this highly-deviated well, readings corresponding to the conductive formation layer are about 30% smaller in magnitude than those in a vertical well. Shoulder effects significantly vary in deviated wells.

---

**Key words** electrostatics – *hp* Finite Elements – exponential convergence – goal oriented adaptivity – through casing resistivity instruments

## 1 Introduction

The design of *quasi-optimal* grids for simulating challenging 3D resistivity logging instruments using mesh-based methods is an involving time-consuming task that is critical for the success of the simulation. Generation of quasi-optimal grids becomes specially difficult when the model contains large variations in resistivity, the dynamic range (ratio between the maximum value and the quantity of interest of the solution) is large, or singularities are strong and may pollute the final result. All these awkward features occur in simulations of through casing resistivity (TCR) measurements.

A number of algorithms have been proposed and utilized by the borehole logging industry to automatically generate *optimal* grids. Among them, we remark the contribution of Druskin and Knizhnerman [2, 3]. Although

they show how to construct grids delivering exponential convergence rates for certain classes of problems and certain quantities of interest, construction of those grids for complicate 3D geometries becomes difficult, and it is unclear whether the speed of convergence that those grids will attain will remain exponential in presence of singularities and/or curved geometries. Another common methodology used by the oil industry consists of transferring 2D-axisymmetric grids (that are easier to construct) to a 3D software. Although this methodology may be efficient and accurate some applications, in this paper we shall prove that it may produce inaccurate results when simulating TCR measurements. Thus, it may lead to erroneous physical interpretations.

As a remedy for these difficulties, in this paper we propose the use of a 3D self-adaptive goal-oriented *hp*-FE method for validation of results. The adaptive algorithm automatically generates an optimal distribution of element size  $h$  and polynomial order of approximation  $p$ , which defines the final *hp*-grid. More precisely, it produces a sequence of grids delivering exponential convergence rates in terms of the CPU time vs. a user-prescribed quantity of interest (in this case, the second vertical difference of the potential). This convergence behavior holds true independently of the number, type, and intensity of singularities present in the solution.

We utilize both methodologies to simulate TCR measurements in deviated wells, and we compare the corresponding results. The paper is a continuation of the work

presented in [8, 10, 11] for 2D TCR problems, and in [9] for 3D laterolog and induction problems. Other methodologies dealing with simulations of 2D TCR measurements can be found in, for example, [14, 15]. However, we are aware of no previous work dealing with computer-aided simulations of 3D TCR measurements.

The remaining of this paper is organized as follows. First, we describe our model TCR problem. This problem is governed by the continuity equation at zero-frequency, that is presented next. Then, we describe our methodology, and we analyze the corresponding numerical results. Conclusions are presented thereafter.

The numerical methodology described in this work can be extended to Alternate Current (AC) logging devices by introducing the so-called edge-elements. The corresponding version is currently under development, and numerical results shall be presented in a forthcoming paper.

## 2 Model Problem of Interest

In this section, we describe our TCR model problem. First, we introduce the zero-frequency form of the continuity equation and an equivalent variational formulation. This equation determines the physics governing our application. Then, we describe the axi-symmetric version of our TCR problem, which is later extended to the final non-axi-symmetric version by introducing an arbitrary dip angle.

### 2.1 DC Resistivity Logging

Direct Current resistivity logging applications are governed by the continuity equation at zero frequency, given by:

$$-\nabla \cdot \bar{\sigma} \nabla u = \nabla \cdot \mathbf{J} , \quad (1)$$

where  $\mathbf{J}$  denotes a prescribed, impressed current source,  $\bar{\sigma}$  is the conductivity tensor, and  $u$  is the electrostatic scalar potential, that is related to the electric field  $\mathbf{E}$  by the formula:

$$\mathbf{E} = -\nabla u . \quad (2)$$

Multiplication of eq. (1) by a test function  $\xi$ , followed by integrating by parts in our computational domain  $\Omega$ , and incorporation of the essential (Dirichlet) and natural (Neumann) boundary conditions defined on  $\Gamma_D$  and  $\Gamma_N$ , respectively, gives rise the following variational problem in terms of the scalar potential  $u$ :

$$\left\{ \begin{array}{l} \text{Find } u \in u_D + H_D^1(\Omega) \text{ such that:} \\ \int_{\Omega} \bar{\sigma} \nabla u \nabla \xi \, dV = \int_{\Omega} \nabla \cdot \mathbf{J} \xi \, dV + \int_{\Gamma_N} g \xi \, dS \quad (3) \\ \forall \xi \in H_D^1(\Omega) , \end{array} \right.$$

where  $H_D^1(\Omega) = \{u \in L^2(\Omega) : u|_{\Gamma_D} = 0, \nabla u \in L^2(\Omega)\}$  is the space of admissible test functions associated with problem (3),  $u_D$  is a lift (typically  $u_D = 0$ ) of the essential boundary condition data  $u_D$  (denoted with the same symbol),  $g = \bar{\sigma} \frac{\partial u}{\partial \mathbf{n}}$  is a prescribed flux on  $\Gamma_N$ , and  $\mathbf{n}$  is the unit normal outward (with respect  $\Omega$ ) vector.

## 2.2 Axi-Symmetric Version of the Simulation Problem

Using cylindrical coordinates  $(\rho, \phi, z)$ , we consider the following geometry, sources, receivers, and materials (described in Figure 1):

- Four (one source and three receivers) 2 cm  $\times$  5 cm ring electrodes located 8 cm from the axis of symmetry and moving along the vertical direction ( $z$ -axis). The receiver electrodes are located 100 cm, 125 cm, and 150 cm above the source electrode, respectively.
- Borehole: a cylinder  $\Omega_A$  of radius 10 cm surrounding the axis of symmetry ( $\Omega_A = \{(\rho, \phi, z) : \rho \leq 10 \text{ cm}\}$ ), with resistivity  $R=0.1 \Omega \cdot \text{m}$ .
- Casing: a pipe (cylindrical shell)  $\Omega_B$  of thickness 1.27 cm surrounding the axis of symmetry ( $\Omega_B = \{(\rho, \phi, z) : 10 \text{ cm} \leq \rho \leq 11.27 \text{ cm}\}$ ), with resistivity  $R=0.0001 = 10^{-5} \Omega \cdot \text{m}$ .
- Formation Material I: a subdomain  $\Omega_C$  defined by  $\Omega_C = \{(\rho, \phi, z) : \rho > 11.27 \text{ cm}, 0 \text{ cm} \leq z \leq 100 \text{ cm}\}$ , with resistivity  $R=10000 \Omega \cdot \text{m}$ .
- Formation Material II: a subdomain  $\Omega_D$  defined by  $\Omega_D = \{(\rho, \phi, z) : \rho > 11.27 \text{ cm}, -50 \text{ cm} \leq z < 0 \text{ cm}\}$ , with resistivity  $R=0.01 \Omega \cdot \text{m}$ .
- Formation Material III: a subdomain  $\Omega_E$  defined by  $\Omega_E = \{(\rho, \phi, z) : \rho > 11.27 \text{ cm}, z < -50 \text{ cm} \text{ or } z > 100 \text{ cm}\}$ , with resistivity  $R=5 \Omega \cdot \text{m}$ .

[Fig. 1 about here.]

## 2.3 Three-Dimensional Problem

At this point, we introduce dip angles of 0, 30, 45, or 60 degrees in order to define our final 3D problem. Simulated measurements consist of the second vertical difference of the scalar potential at the receiver electrodes, given by the formula

$$L(u) = \frac{\int_{\Omega_1} u(x) dx}{\int_{\Omega_1} 1 dx} - \frac{2 \int_{\Omega_2} u(x) dx}{\int_{\Omega_2} 1 dx} + \frac{\int_{\Omega_3} u(x) dx}{\int_{\Omega_3} 1 dx}, \quad (4)$$

where  $L$  denotes our quantity of interest, which is a linear and continuous functional in  $H_D^1(\Omega)$ , and  $\Omega_i$  denotes the subdomain occupied by the  $i$ -th receiver electrode.  $L(u)$  is proportional to the leakage of current into the formation — see [4] —, and thus, it is expected to be proportional to the formation conductivity.

The main objective in our simulations is to study the sensitivity of the measurements to the dip angle between the axis of the borehole and the transversed layer.

## 3 Methodology

Our numerical technique is based on  $hp$ -FE discretizations of elliptic problems. Here  $h$  stands for element size, and  $p$  denotes the polynomial element order (degree) of approximation, both varying *locally* throughout the grid.

In order to obtain accurate measurement simulations, we construct 3D  $hp$ -grids using two different self-adaptive goal-oriented  $hp$ -adaptive strategies. These strategies are based on 2D and 3D algorithms, respectively. First, we

describe the 3D self-adaptive strategy. Then, we describe the construction of 3D grids based on 2D algorithms.

### 3.1 3D Self-Adaptive Strategy

We define a function  $G \in H_D^1(\Omega)$  solution of the following variational formulation:

$$\int_{\Omega} \bar{\sigma} \nabla \xi \nabla G \, dV = L(\xi) \quad \forall \xi \in H_D^1(\Omega). \quad (5)$$

Eq. (5) provides a representation formula that specifies how much an arbitrary subdomain (or element) of  $\Omega$  contributes to the quantity of interest of the solution  $L(u)$ . Thus, it allows for the construction of a goal-oriented adaptive algorithm intended to approximate only  $L(u)$  — as opposed to approximate  $u$  over the entire computational domain — (see [8, 13] for details on goal-oriented adaptive algorithms).

At this point, we describe an algorithm for the construction of an optimal goal-oriented  $hp$ -grid. First, we generate a human-made initial  $hp$ -grid. Then, we iterate along the following steps:

1. Given an arbitrary  $hp$ -grid — that we shall denote as *coarse-grid* — we solve variational problems (3) and (5).
2. We perform a global  $hp$ -refinement to obtain the corresponding  $h/2, p+1$ -grid, that is obtained from the coarse grid by breaking all elements into eight new elements, and raising the polynomial order of approximation,  $p$ , uniformly by 1. We shall denote the resulting grid as the *fine-grid*.

3. We solve problems (3) and (5) on the fine-grid with a two-grid solver [6], and we estimate the coarse-grid error by computing the difference between fine-grid and coarse-grid solutions. If the computed coarse-grid error estimation is below the desired error tolerance, then we stop our iterations and provide the fine-grid solution as the ultimate result. The fine-grid solution error is expected to be about one or two orders of magnitude smaller than the estimated coarse-grid error.
4. We utilize the fine grid solution  $L(u)$  to guide optimal refinements over the coarse grid. More precisely, we utilize the projection-based interpolation operator  $\Pi$  defined in [1] to pose the following optimization problem:

$$\left\{ \begin{array}{l} \text{Find an optimal } \tilde{hp}\text{-grid in the following sense:} \\ \tilde{hp} = \arg \max_{\widehat{hp}} \sum_K \frac{\|u - \Pi_{hp} u\|_K^2 \cdot \|G - \Pi_{hp} G\|_K^2}{\Delta N} \\ \quad - \frac{\|u - \Pi_{\widehat{hp}} u\|_K^2 \cdot \|G - \Pi_{\widehat{hp}} G\|_K^2}{\Delta N}, \end{array} \right. \quad (6)$$

where

- $u = u_{\frac{h}{2}, p+1}, G = G_{\frac{h}{2}, p+1}$  are the fine-grid solutions of problems (3) and (5), respectively,
- $K$  indicates an element, and
- $\Delta N > 0$  is the increment in the number of unknowns from coarse grid  $hp$  to the intermediate grid  $\widehat{hp}$ .

This maximization problem is solved by executing an algorithm based on the sequential optimization of edges, faces, and interiors of elements. This algorithm, which is quite involved [5], produces a list of elements to be refined, as well as their corresponding optimal refinements.

5. We execute optimal refinements as determined in the previous step in order to construct our next *optimal* coarse-grid. At this point, we discard the fine-grid.

As a final result, we provide a coarse-grid error estimation accompanied with the corresponding fine-grid solution.

### 3.2 2D Self-Adaptive Strategy for 3D Problems

In this method, we construct our *hp*-grid by following the next steps: First, we automatically generate a 2D optimal *hp*-grid for axi-symmetric problems by utilizing the self-adaptive goal-oriented *hp*-FE method described in [7, 8, 11, 12]. Second, we transfer the optimal 2D grid to the 3D *hp*-FE software, by employing either four or eight second-order elements in the azimuthal direction. Third, the resulting 3D *hp*-FE grid is tilted to account for deviated wells. Finally, and after solving our problem of interest within the 3D *hp*-FE software setting, an analysis of the error is performed by considering a finer (globally *p*-refined) three-dimensional grid and comparing results obtained with the two grids.

In both methods described above, we combine the use of *hp*-FE discretizations with exact geometry elements and conformal grids. Thus, we avoid geometry-induced numerical errors.

## 4 Numerical Results

In this section, we compare the performance of the two numerical methodologies described above when applied to our TCR model problem. In addition, numerical simulations allow us to study physical effects occurring in TCR measurements acquired in deviated wells.

First, we consider our axisymmetric TCR model problem in a vertical well. We solve the problem in two-dimensions, and in three-dimensions using the two methodologies described in this paper. In Figure 2 — left panel —, we display the simulated measurements obtained by utilizing the following methods: 1) the 2D software [8] (triangles), 2) a 2D optimal grid transferred to the 3D software (circles), and 3) a 2D optimal grid transferred to the 3D software and globally enriched by a *p*-refinement (solid line). In all cases, we obtain almost identical results. More precisely, the numerical error remains below 1%, as displayed in Figure 2 — right panel —.

[Fig. 2 about here.]

In figures 3 and 4, we describe similar results for the thirty-degrees and sixty-degrees deviated well, respectively. Specifically, in the left panel we display the simulated measurements obtained by utilizing the following

methods: 1) the 2D software [8] (triangles), 2) the 2D optimal grid transferred to the 3D software (circles), 3) the 2D optimal grid transferred to the 3D software and globally enriched by a  $p$ -refinement (solid line), and 4) the 3D optimal grid obtained by executing the 3D self-adaptive goal-oriented  $hp$ -FEM (dashed line with '+'). In the right panel we display the numerical relative error with respect to the solution obtained using the 3D self-adaptive goal-oriented  $hp$ -FEM. We utilize this reference solution, since the difference between that  $hp$ -solution and the solution in a globally  $hp$ -unrefined grid (that is, in the  $2h, p-1$ -grid) indicates that the relative error remains below 5%. We note that a grid providing errors below 1% in vertical wells may deliver large errors (over 300%) in deviated wells.

[Fig. 3 about here.]

[Fig. 4 about here.]

In Figure 5, we display the relative difference in percentage between the solutions corresponding to the grid obtained with the 3D self-adaptive  $hp$ -algorithm and the 2D solution. For the most resistive layer ( $1000 \Omega \cdot \text{m}$ ), the effect of dip angle increases the solution by about 50% and 2000%, for the 30 and 60 degrees deviated well, respectively. In the most conductive layer ( $0.01 \Omega \cdot \text{m}$ ), these differences are greatly reduced to 6% and 20%, respectively. Nevertheless, we observe a large relative difference on the shoulder effect at the bottom of the conductive layer.

[Fig. 5 about here.]

In Figure 6 we display the final coarse  $hp$ -grid obtained with the 2D algorithm and transferred to the 3D software along with the corresponding solution. We observe a variety of refinements, mainly around the transmitter and the three receiver electrodes. In the solution graphic, we note that the potential propagates throughout the casing, while it dissipates within the formation as the radial distance from the axis of symmetry increases.

[Fig. 6 about here.]

## 5 Conclusions

In this paper we have simulated 3D TCR measurements with two different methodologies for constructing *optimal* grids. Numerical results illustrate that the methodology based on constructing optimal 2D grids and transferring them to the 3D software provides inaccurate results when simulating TCR measurements in deviated wells.

Thus, we have employed a second methodology based on a 3D self-adaptive goal-oriented  $hp$ -adaptive algorithm. This methodology, although computationally less efficient, provides accurate simulations that are verified by a built-in *a posteriori* error estimator based on the solution of the problem in a finer-grid.

Simulated TCR measurements indicate a large sensitivity with respect to the dip angle. Specifically, relative differences between measurements in a vertical well and

in a sixty-degrees deviated well are as large as 3000%. These differences are especially large in highly resistive formations.

*Acknowledgements* This work was financially supported by Baker Atlas and The University of Texas at Austin's *Joint Industry Research Consortium on Formation Evaluation* sponsored by Aramco, Baker Atlas, BP, British Gas, Chevron, ConocoPhillips, ENI E&P, ExxonMobil, Halliburton, Marathon, Mexican Institute for Petroleum, Norsk-Hydro, Occidental Petroleum, Petrobras, Schlumberger, Shell E&P, Statoil, TOTAL, and Weatherford International Ltd.

The third author was financially supported by the Foundation for Polish Science under program Homing.

## References

1. L. Demkowicz and A. Buffa.  $H^1$ ,  $H(\text{curl})$ , and  $H(\text{div})$  conforming projection-based interpolation in three dimensions: quasi optimal  $p$ -interpolation estimates. *Computer Methods in Applied Mechanics and Engineering*, 194:267–296, 2005.
2. V. Druskin and L. Knizhnerman. Gaussian spectral rules for the three-point second differences: I. A two-point positive definite problem in a semi-infinite domain. *SIAM Journal of Numerical Analysis*, 37:403–422, 1999.
3. V. Druskin and L. Knizhnerman. Gaussian spectral rules for second order finite-difference schemes. *Numerical Algorithms*, 25:139–159, 2000.
4. A. A. Kaufman. The electrical field in a borehole with casing. *Geophysics*, 55(1):29–38, 1990.
5. J. Kurtz and L. Demkowicz. A fully automatic hp-adaptivity for elliptic PDEs in three dimensions. *Submitted to Computer Methods in Applied Mechanics and Engineering*, 2006.
6. D. Pardo and L. Demkowicz. Integration of hp-adaptivity with a two grid solver for elliptic problems. *Computational Methods on Applied Mechanics and Engineering (CMAME)*, 195, 2006.
7. D. Pardo, L. Demkowicz, C. Torres-Verdin, and M. Paszynski. Simulation of resistivity logging-while-drilling (LWD) measurements using a self-adaptive goal-oriented hp-finite element method. *SIAM Journal on Applied Mathematics*, 66:2085–2106, 2006.
8. D. Pardo, L. Demkowicz, C. Torres-Verdin, and L. Tabarovsky. A goal-oriented hp-adaptive finite element method with electromagnetic applications. Part I: electrostatics. *Int. J. Numer. Methods Eng.*, 65:1269–1309, 2006.
9. D. Pardo, M. Paszynski, C. Torres-Verdin, and L. Demkowicz. Simulation of 3D DC borehole resistivity measurements with a goal-oriented hp-finite element method. Part I: laterolog and LWD. *Submitted to IEEE Geosciences and Remote Sensing Letters*. Preprint available at: [www.ices.utexas.edu/%7Epardo](http://www.ices.utexas.edu/%7Epardo), 2006.
10. D. Pardo, C. Torres-Verdin, and L. Demkowicz. Feasibility Study for Two-Dimensional Frequency Dependent Electromagnetic Sensing Through Casing. *In press at: Geophysics*. Preprint available at: [www.ices.utexas.edu/%7Epardo](http://www.ices.utexas.edu/%7Epardo), 2006.
11. D. Pardo, C. Torres-Verdin, and L. Demkowicz. Simulation of multi-frequency borehole resistivity measure-

- ments through metal casing using a goal-oriented  $hp$ -finite element method. *IEEE Transactions on Geosciences and Remote Sensing*, 44:2125–2135, 2006.
12. M. Paszynski, L. Demkowicz, and D. Pardo. Verification of goal-oriented  $hp$ -adaptivity. *Computers and Mathematics with Applications*, 50:1395–1404, 2005.
  13. S. Prudhomme and J. T. Oden. On goal-oriented error estimation for elliptic problems: application to the control of pointwise errors. *Computer Methods in Applied Mechanics and Engineering*, 176(1-4):313–331, 1999.
  14. C. J. Schenkel and H. F. Morrison. Electrical resistivity measurement through metal casing. *Geophysics*, 59(7):1072–1082, 1994.
  15. X. Wu and T. M. Habashy. Influence of steel casings on electromagnetic signals. *Geophysics*, 59(3):378–390, 1994.

**List of Figures**

1	2D cross-section of the geometry of the TCR problem. Measurements are based on one transmitter and three receiver electrodes. The rock formation is composed of four different layers with varying conductivities. . . . .	11
2	Simulation of TCR measurements in a vertical well. Left panel: final solution. Right panel: final relative error with respect to the 2D solution. Different curves identify the following results: A) Triangles: results obtained with the 2D <i>hp</i> -FE software. B) Discontinuous line with circles: results obtained using an optimal 2D <i>hp</i> -FE grid transferred to the 3D software. C) Solid line: results obtained with an optimal 2D <i>hp</i> -FE grid transferred to the 3D software, and increase globally the polynomial order of approximation $p$ by one. . . . .	12
3	Simulation of TCR measurements in a thirty-degrees deviated well. Left panel: final solution. Right panel: final relative error with respect to the 3D-adapt solution. Different curves identify the following results: A) Triangles: results obtained with the 2D <i>hp</i> -FE software. B) Discontinuous line with circles: results obtained using an optimal 2D <i>hp</i> -FE grid transferred to the 3D software. C) Solid line: results obtained with an optimal 2D <i>hp</i> -FE grid transferred to the 3D software, and increase globally the polynomial order of approximation $p$ by one. . . . .	13
4	Simulation of TCR measurements in a sixty-degrees deviated well. Left panel: final solution. Right panel: final relative error with respect to the 3D-adapt solution. Different curves identify the following results: A) Triangles: results obtained with the 2D <i>hp</i> -FE software. B) Discontinuous line with circles: results obtained using an optimal 2D <i>hp</i> -FE grid transferred to the 3D software. C) Solid line: results obtained with an optimal 2D <i>hp</i> -FE grid transferred to the 3D software, and increase globally the polynomial order of approximation $p$ by one. . . . .	14
5	Simulation of TCR measurements in a deviated well. We display the relative difference with respect to the 2D solution. Different curves correspond to difference dip angles: 30 degrees and 60 degrees, respectively. Optimal grids have been constructed by utilizing a 3D self-adaptive goal-oriented <i>hp</i> -finite element method. . . . .	15
6	Simulation of TCR measurements in a sixty-degrees deviated well. Top panel: Final <i>hp</i> -grid generated with the 2D self-adaptive software, and transferred to three dimensions. Different colors indicate different polynomial orders of approximation. Bottom panel: Final solution (scalar potential). . . . .	16

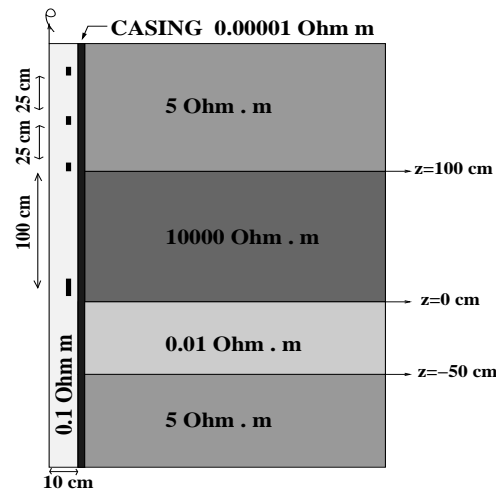


**Fig. 1** 2D cross-section of the geometry of the TCR problem. Measurements are based on one transmitter and three receiver electrodes. The rock formation is composed of four different layers with varying conductivities.

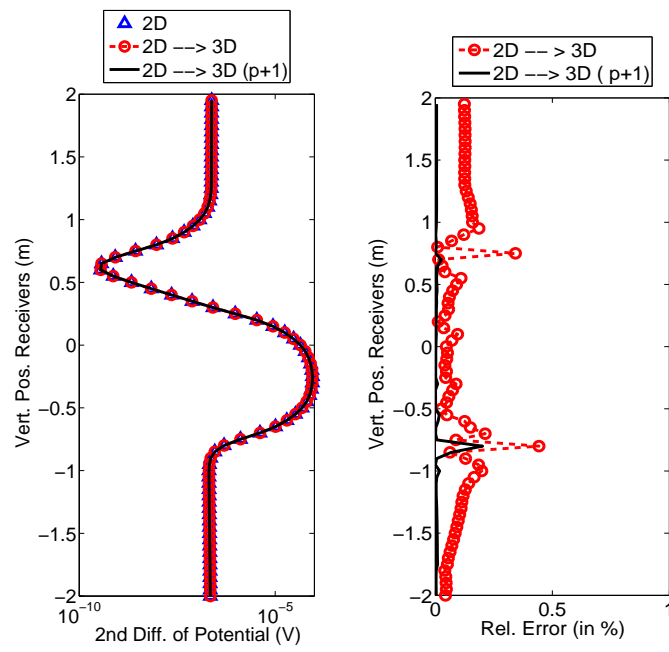


**Fig. 2** Simulation of TCR measurements in a vertical well. Left panel: final solution. Right panel: final relative error with respect to the 2D solution. Different curves identify the following results: A) Triangles: results obtained with the 2D  $hp$ -FE software. B) Discontinuous line with circles: results obtained using an optimal 2D  $hp$ -FE grid transferred to the 3D software. C) Solid line: results obtained with an optimal 2D  $hp$ -FE grid transferred to the 3D software, and increase globally the polynomial order of approximation  $p$  by one.

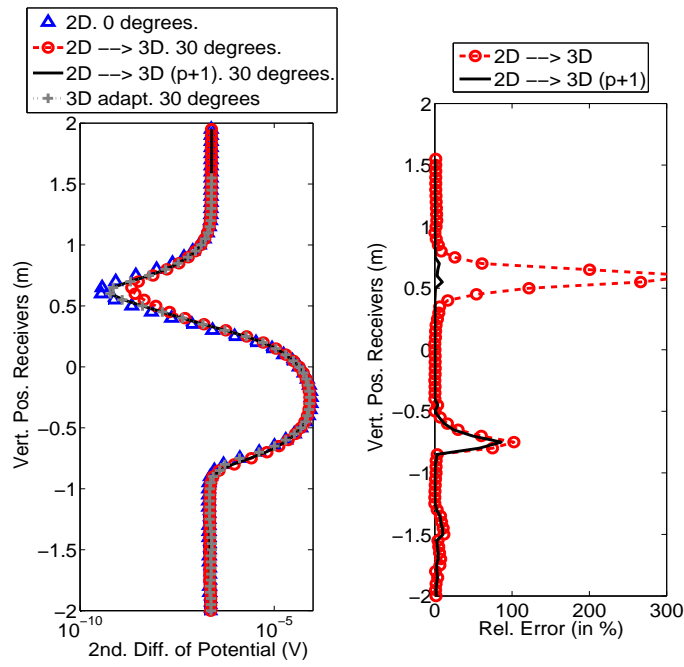


**Fig. 3** Simulation of TCR measurements in a thirty-degree deviated well. Left panel: final solution. Right panel: final relative error with respect to the 3D-adapt solution. Different curves identify the following results: A) Triangles: results obtained with the 2D *hp*-FE software. B) Discontinuous line with circles: results obtained using an optimal 2D *hp*-FE grid transferred to the 3D software. C) Solid line: results obtained with an optimal 2D *hp*-FE grid transferred to the 3D software, and increase globally the polynomial order of approximation  $p$  by one.

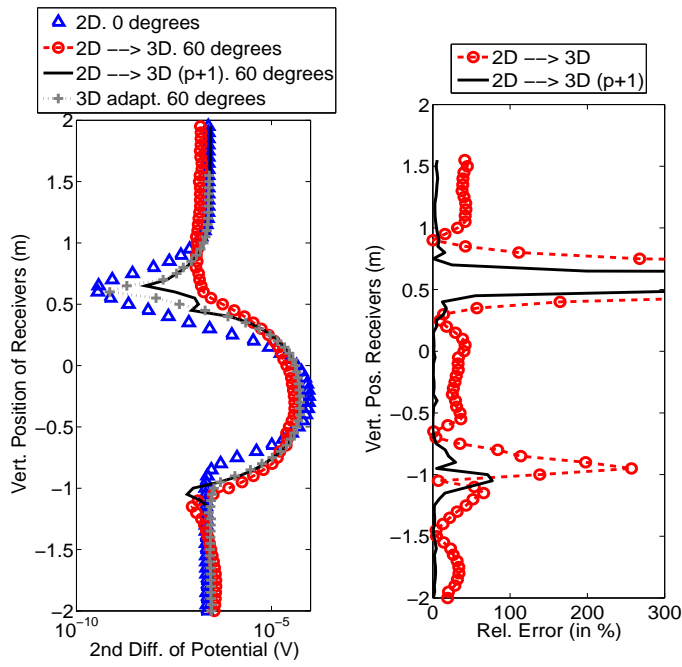


**Fig. 4** Simulation of TCR measurements in a sixty-degree deviated well. Left panel: final solution. Right panel: final relative error with respect to the 3D-adapt solution. Different curves identify the following results: A) Triangles: results obtained with the 2D  $hp$ -FE software. B) Discontinuous line with circles: results obtained using an optimal 2D  $hp$ -FE grid transferred to the 3D software. C) Solid line: results obtained with an optimal 2D  $hp$ -FE grid transferred to the 3D software, and increase globally the polynomial order of approximation  $p$  by one.

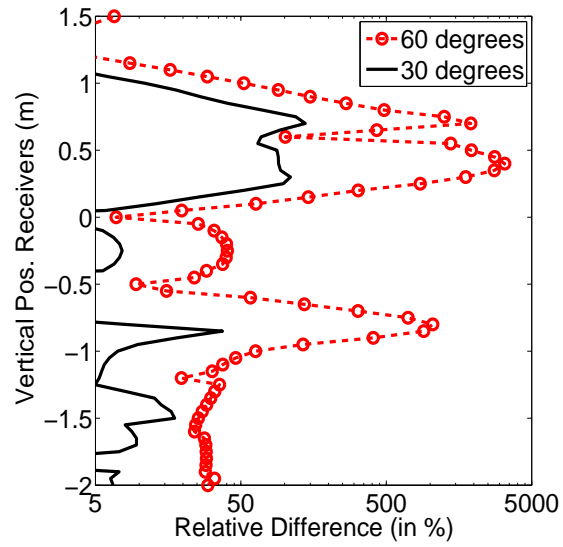


**Fig. 5** Simulation of TCR measurements in a deviated well. We display the relative difference with respect to the 2D solution. Different curves correspond to difference dip angles: 30 degrees and 60 degrees, respectively. Optimal grids have been constructed by utilizing a 3D self-adaptive goal-oriented *hp*-finite element method.

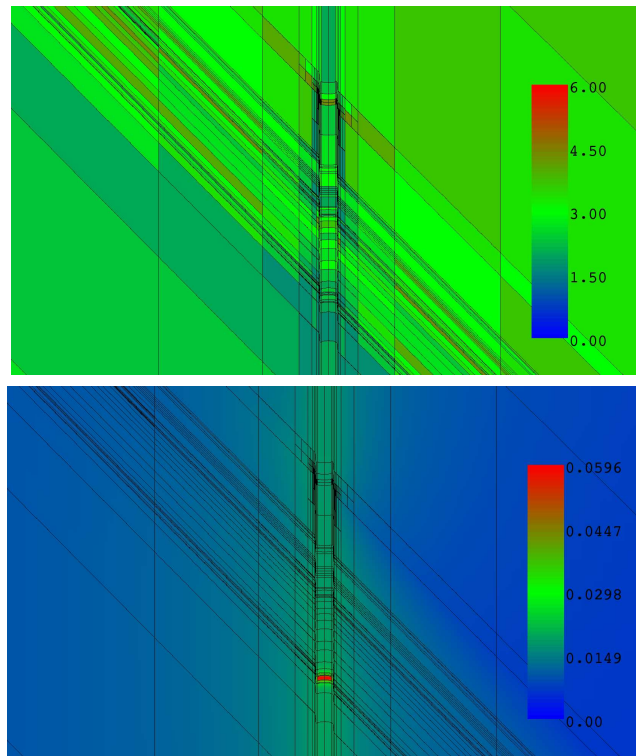


**Fig. 6** Simulation of TCR measurements in a sixty-degree deviated well. Top panel: Final  $hp$ -grid generated with the 2D self-adaptive software, and transferred to three dimensions. Different colors indicate different polynomial orders of approximation. Bottom panel: Final solution (scalar potential).